# Elastic scattering of alpha particles near the Coulomb barrier and matter distribution of medium and heavy nuclei

I. Badawy,* B. Berthier, P. Charles, M. Dost, † B. Fernandez, J. Gastebois, and S. M. Lee‡
*Département de Physique Nucléaire CEN Saclay, BP 2, 91190 Gif-sur-Yvette, France*
(Received 6 July 1977)

The elastic scattering of $\alpha$ particles near 180° was measured in the vicinity of the Coulomb barrier for $^{110,112,114,116}$Cd, $^{112,114,116,118,120,122,124}$Sn, $^{122,124,126,128,130}$Te, $^{144,148,150,152}$Sm, and $^{204,206,208}$Pb. An optical-model analysis using Woods-Saxon potentials shows that the usual parameters of the real part of the potential $V$, $R_{opt}$ and $a$ must obey the relationship $V \exp[(R_{opt} - R_{0.2})/a] = 0.2$ MeV in order to fit the data. The $\alpha$-nucleus distance $R_{0.2}$ at which the nuclear potential depth is $-0.2$ MeV can then be determined for each nucleus within $\pm 0.03$ fm. An analysis in terms of a folding model was performed for $^{208}$Pb and $^{124}$Te. For the class of potentials thus obtained, it is the $\alpha$-nucleus distance at 0.5 MeV depth rather than at 0.2 MeV that appears to be best determined. The same analysis determines the radius $R_{FD=0.002}$ at which the nucleon density is $2\times10^{-3}$ nucleon/fm$^3$. The value of $R_{FD}$ is found to depend mostly on the $\alpha$-nucleon effective interaction used, and very little on the functional form of the density distribution. Further evidence is presented in favor of the Gaussian interaction $-U_0 \exp(-K^2r^2)$ with $U_0 = 127$ MeV and $K = 0.6$ fm$^{-1}$, which has been proposed by Sumner and which leads to the probable value $R_{FD} = R_{0.2} - (3.06 \pm 0.03)$ fm. Other interactions are not excluded, however, and considering those proposed so far in the literature leads to $R_{FD} = R_{0.2} - (3.11 \pm 0.14)$ fm. The average variation of $R_{FD}$ with mass number is found to be $\langle R_{FD} \rangle = (1.355A^{1/3} + 0.87)$ fm for spherical nuclei. The rate of variation of $\langle R_{FD} \rangle$ with mass number is found to be in good agreement with the droplet model predictions, which is taken as an evidence that the surface thickness of spherical nuclei is practically constant from Sn to Pb.

## I. INTRODUCTION

The elastic scattering of $\alpha$ particles has been used extensively at energies well above the Coulomb barrier to investigate the size of atomic nuclei. At these energies use was made of the strongly diffractional character of this scattering in order to determine a strong absorption radius.[1] Several authors then pointed out that, at the strong absorption radius, the depth of the real part of the nuclear potential felt at a given energy by the incoming $\alpha$ particle depends very little on the possible ambiguities in the parameters of this potential. Typical such depths were found to be $-1.9$ MeV for $^{42}$Ca and $^{50}$Ti at 30.5 MeV, $-2.4$ MeV for a series of Ca, Ti, and Ni isotopes at 42 MeV.[2,3] The strong absorption radius is then considered as a most significant size parameter.

It is only in the last few years that the original Rutherford method,[4] viz., elastic scattering of $\alpha$ particles near the Coulomb barrier at large angles was again utilized. Several authors have done such measurements at a series of angles and have defined, on the basis of optical-model analyses, some quantities as significant size parameters. Goldring *et al.*[5] and Eisen *et al.*[6] have proposed the radius at which the sum of Coulomb plus real nuclear potential is maximum, which they call the Rutherford radius $R_R$, and Tabor, Watson, and Hansen[7] have in addition proposed the radius $R_{cf}$ where the nuclear potential amounts to the constant fraction of 2% of the Coulomb potential.

In the present work, we have measured the cross section of $\alpha$ particles elastically scattered from $^{110,112,114,116}$Cd, $^{112,114,116,118,120,122,124}$Sn, $^{122,124,126,128,130}$Te, $^{144,148,150,152}$Sm, and $^{204,206,208}$Pb at energies near the Coulomb barrier and at one single angle near 180°. The choice of the largest possible angle was motivated by the remark that in such experiments we study the first effects of the interference between the nuclear amplitude and the Coulomb amplitude when the energy is increased from below the Coulomb barrier to a few MeV above it. Since the Coulomb amplitude decreases very rapidly with increasing angle, the interference with a small nuclear amplitude is maximum at 180°. Furthermore, we shall show later on that additional measurements at other angles would not give any further information on the $\alpha$-nucleus potential.

After a description of the experimental arrangement and procedure in Sec. II, the optical-model analysis of the data is presented in Sec. III, where we shall show that for incident energies close to the Coulomb barrier the $\alpha$-nucleus distance $R_{0.2}$ at which the real nuclear potential is 0.2 MeV

deep is the most significant quantity characterizing the scattering process. What this implies for the nuclear matter distribution is discussed in Sec. IV, where we shall show that the best defined quantity is the radius $R_{FD}$ where the nuclear density is $2.10^{-3}$ nucleon/fm$^3$. Finally we relate in Sec. V our results to other information on the nucleon density distribution.

## II. EXPERIMENTAL ARRANGEMENT AND PROCEDURE

The beam of $\alpha$ particles was produced by the FN tandem Van de Graaff accelerator of the CEN Saclay with a typical intensity on target of about 200 nA. An annular silicon surface barrier detector of 150 mm$^2$ surface area and 400 $\mu$m depth was mounted at the entrance of the scattering chamber. The detector was protected against the beam by an assembly of tantalum diaphragms and a funnel-shaped piece of tantalum. The smallest diaphragm was 3 mm in diameter. The detector was situated at 170 mm from the target, subtending a solid angle of 1.74 msr at 178.6 $\pm 0.3°$. Another silicon surface barrier detector of 100 mm$^2$ surface area and 1000 $\mu$m depth was mounted at 30° for monitoring. In order to suppress backscattering into the annular detector, the beam was stopped in a beryllium plate mounted inside the Faraday cup.

The targets (enriched isotopes supplied by ORNL) were prepared by evaporation under vacuum on a 10 $\mu$g/cm$^2$ carbon backing. A 2 to 5 $\mu$g/cm$^2$ gold layer was deposited onto the cadmium, tin, and tellurium targets for monitoring purposes as explained below. Table I lists the target thickness and isotopic composition for the 23 isotopes studied in this work. In the cases of the rare isotopes of $^{112}$Sn, $^{124}$Te, $^{148}$Sm, and $^{204}$Pb admixtures of the more abundant isotopes of the same element were sufficiently large so as to render corrections of the measured counting rates necessary. The elastic cross sections measured with the highly enriched targets of these isotopes were used for these corrections, which in no case amounted to more than 1%.

For target nuclei much lighter than gold, viz., cadmium, tin, and tellurium isotopes, monitoring was done by measuring simultaneously the scat-

TABLE I. Isotopic purity and thickness of targets used in this work.

| Nuclide | Thickness ($\mu$g/cm$^2$) | Enrichment (%) | Contaminations (%) |
|---|---|---|---|
| $^{110}$Cd | 50 | 97.2 ± 0.05 | 1.04 of $^{111}$Cd, 0.9 of $^{112}$Cd |
| $^{112}$Cd | 50 | 97.8 ± 0.1 | 0.73 of $^{113}$Cd, 0.71 of $^{114}$Cd |
| $^{114}$Cd | 50 | 99.09 ± 0.05 | Traces of $^{112}$Cd, $^{113}$Cd |
| $^{116}$Cd | 50 | 97.2 ± 0.1 | 1.44 of $^{114}$Cd |
| $^{112}$Sn | 40 | 83.64 ± 0.04 | 3.9 of $^{116}$Sn, 3.61 of $^{120}$Sn |
| $^{114}$Sn | 40 | 60.65 ± 0.2 | 11.99 of $^{116}$Sn, 3.72 of $^{117}$Sn, 6.89 of $^{118}$Sn, 2.0 of $^{119}$Sn, 11.07 of $^{120}$Sn |
| $^{116}$Sn | 40 | 95.74 ± 0.05 | 1.02 of $^{117}$Sn, 1.48 of $^{118}$Sn, 1.06 of $^{120}$Sn |
| $^{118}$Sn | 40 | 97.1 ± 0.2 | 1.1 of $^{119}$Sn, 1.2 of $^{120}$Sn |
| $^{120}$Sn | 40 | 98.39 ± 0.05 | Traces of $^{118}$Sn, $^{119}$Sn, $^{124}$Sn |
| $^{122}$Sn | 40 | 90.8 ± 0.1 | 1.01 of $^{116}$Sn, 1.91 of $^{118}$Sn, 3.75 of $^{120}$Sn, 1.16 of $^{124}$Sn |
| $^{124}$Sn | 40 | 96.0 ± 0.1 | 1.2 of $^{120}$Sn, 1.2 of $^{122}$Sn |
| $^{122}$Te | 50 | 95.44 ± 0.1 | 1.03 of $^{130}$Te |
| $^{124}$Te | 50 | 83.7 ± 0.1 | 8.5 of $^{125}$Te, 3.3 of $^{126}$Te, 2.2 of $^{128}$Te, 1.7 of $^{130}$Te |
| $^{126}$Te | 50 | 97.0 ± 0.2 | 1.0 of $^{128}$Te, 1.0 of $^{130}$Te |
| $^{128}$Te | 50 | 99.46 ± 0.1 | 0.48 of $^{130}$Te |
| $^{130}$Te | 50 | 99.49 ± 0 | Trace of $^{128}$Te |
| $^{144}$Sm | 60 | 95.1 ± 0.1 | 1.45 of $^{147}$Sm, 0.93 of $^{152}$Sm |
| $^{148}$Sm | 60 | 76.01 ± 0.05 | 3.0 of $^{147}$Sm, 0.62 of $^{154}$Sm |
| $^{150}$Sm | 60 | 94.1 ± 0.05 | 3.3 of $^{152}$Sm |
| $^{152}$Sm | 60 | 99.06 ± 0.05 | 0.48 of $^{154}$Sm |
| $^{204}$Pb | 250 | 71.1 ± 0.1 | 13.3 of $^{206}$Pb, 5.8 of $^{207}$Pb, 9.82 of $^{208}$Pb |
| $^{206}$Pb | 400 | 97.2 ± 0.05 | 1.34 of $^{207}$Pb, 1.39 of $^{208}$Pb |
| $^{208}$Pb | 400 | 99.3 ± 0.05 | Traces of $^{206}$Pb, $^{207}$Pb. |

tered $\alpha$ particles from the isotope under study and the thin gold layer. Since the $\alpha$-Au scattering follows the Rutherford law at the energies considered here, and has therefore an $E_\alpha^{-2}$ dependence upon the $\alpha$-particle energy $E_\alpha$, the ratio of the two counting rates is proportional to the ratio $\sigma_{el}/\sigma_R$ of the elastic to the Rutherford cross section for the isotope considered. The absolute normalization was then simply given by the measurements well below the Coulomb barrier where $\sigma_{el}/\sigma_R = 1$. As for the heavier targets, this procedure has to be modified since the $\alpha$-Au scattering is no longer of Rutherford type at the energies required to pass the Sm + $\alpha$ or Pb + $\alpha$ Coulomb barriers.

In all cases, however, the grazing angle is at least about 90° at the highest energies (see Fig. 6), and optical-model calculations show that $\sigma_{el}(30°) = \sigma_R(30°)$ to within less than 1%, a result that was confirmed within its accuracy of 2 to 3% by integrated beam current monitoring. Consequently $\sigma_{el}(30°)$ as measured by the monitor counter was used as reference cross section. Finally, statistics better than 1% were obtained in most cases.

Measurements were carried out on the following targets for the incident laboratory energies as indicated:

$^{110,112,114,116}$Cd from 8 to 17 MeV,

$^{112,114,116,118,120,122,124}$Sn from 8 to 17 MeV,

$^{122,124,126,128,130}$Te from 8 to 17 MeV,

$^{144,148,150,152}$Sm from 10 to 20 MeV,

$^{204,206,208}$Pb from 15 to 23 MeV.

Energy steps ranged from 0.25 to 1 MeV. Examples of the results appear in Fig. 1.

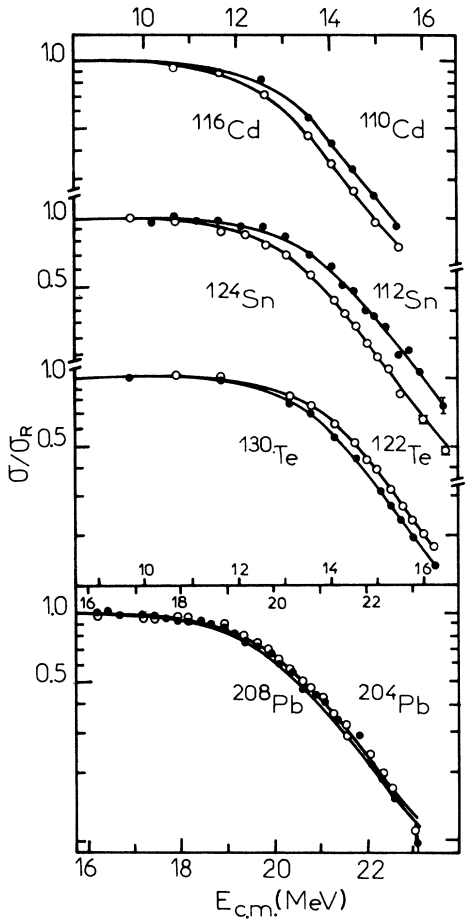


FIG. 1. Typical excitation functions measured at 179°. Solid lines are optical model fits.

## III. OPTICAL MODEL ANALYSIS AND DISCUSSION

### A. Woods-Saxon analysis of present data

An optical-model analysis of the results described in Sec. II was carried out using a standard four-parameter optical model

$$U(r) = -(V + iW)/\{1 + \exp[(r - R_{opt})/a]\}.$$

The quality of the fit is excellent, as can be seen on the excitation functions at 179° shown in Fig. 1. However, none of the parameters defining $U(r)$ can be unambiguously determined by the fit of the elastic scattering cross sections. We are going to show that only a relationship between $V$, $R_{opt}$, and $a$ can be established on the basis of these data, but that it turns out to be possible to extract a well defined interaction distance from the data.

First, the results are very insensitive to the value of $W$, as can be seen in the examples shown in Fig. 2, where the $\chi^2$ for three typical cases is shown as a function of $W$, all other parameters being fixed. It can be seen that the quality of the fit is changed very little provided $W$ is larger than

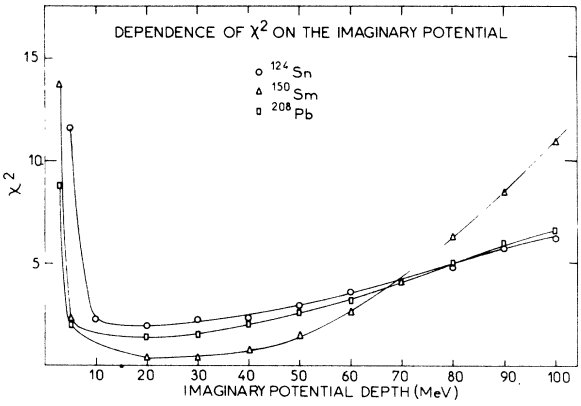


FIG. 2. Variation of the $\chi^2$ when the imaginary part of the potential varies, all other parameters being kept fixed.

10 MeV and not larger than about 80 MeV. This pattern is very general for all nuclei under study. For $W$ smaller than about 10 MeV, the $\chi^2$ has a very rapid increase, and a very slow increase after a flat minimum at around 10–40 MeV. Consequently, we fixed $W$ at 20 MeV for all analyses.

Secondly, when $W$ and $a$ were kept fixed, it was found that the Igo ambiguity[8] is extremely well satisfied for a continuous family of $R_{opt}$ and $V$, i.e., the fit is maintained provided

$$V \exp(R_{opt}/a) = \text{const.} \quad (1)$$

For example, best fits obtained on $^{124}$Sn for $W = 20$ MeV, $a = 0.57$ fm, and $V$ ranging from 100 to 300 MeV yielded values of $R_{opt}$ such that the value of $V \exp(R_{opt}/a)$ varied by less than 0.3%. This simply means that the scattering cross sections are sensitive only to the far-out tail of the real part of the nuclear potential, where $r \gg R_{opt}$, so that $\exp[(r - R_{opt})/a] \gg 1$, therefore

$$V\{1 + \exp[(r - R_{opt})/a]\}^{-1} \simeq V \exp(R_{opt}/a) \exp(-r/a) .$$

Thus all combinations of $V$ and $R_{opt}$ that satisfy relation (1) define constant potentials with the same tail for distances $r \gg R_{opt}$. The fact that relation (1) is well satisfied in the present case therefore implies that the scattering process depends only on the fringe region of the real part of the projectile-target potential whose radial shape varies like $\exp(-r/a)$. Such is the case for a real potential of Woods-Saxon shape in strong absorption situations.

Third, after having observed the Igo relationship and the insensitivity of the fits to the precise depth of the absorptive potential $W$ (that is kept equal to 20 MeV), we are left with the problem to choose $a$, after having fixed $V$ to the plausible, but to a large extent arbitrary, value of 200 MeV. A choice of $a$ implies one of $R_{opt}$ through the validity of the Igo relationship (1). However, the present data do not favor any particular value of $a$ among the ones we have used, and which comprise the most commonly accepted ones. This point is illustrated in Fig. 3, where calculations with different values of $R_{opt}$ and $a$ are compared to a *standard* calculation (full line) of the $^{208}$Pb excitation function at 180°. The parameters of this *standard* calculation (which give a good fit to the data) are $V = 200$ MeV, $W = 20$ MeV, $R_{opt} = 8.03$ fm, and $a = 0.57$ fm. The upper group of curves shows that a change of $R_{opt}$ or $a$ introduces only a shift of the excitation function towards higher or lower energy. An identical shift towards higher energies is obtained by changing $a$ by +0.05 fm or $R_{opt}$ by −0.32 fm. A corresponding shift towards lower energies is obtained by changing $a$ by −0.05 fm or $R_{opt}$ by +0.33 fm. The lower curves of Fig. 3

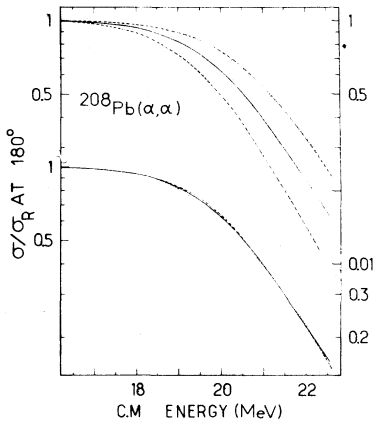


FIG. 3. Calculated excitation functions at 180° for the $^{208}$Pb case. The values of $V$ and $W$ have been kept fixed to 200 and 20 MeV, respectively. The full curves correspond to the *standard* values of $R_{opt}$ and $a$, 8.03 and 0.57 fm, respectively. The upper set of curves shows that almost identical results are obtained either when $a$ is changed by ±0.05 fm, or when $R_{opt}$ is changed by −0.32 or +0.33 fm, respectively (dashed lines). The lower curves show that when these changes are done simultaneously, one gets excitation curves almost identical to the *standard* one. The dashed curve corresponds to $a = 0.52$ fm and $R_{opt} = 8.36$ fm while the dotted curve corresponds to $a = 0.62$ fm and $R_{opt} = 7.71$ fm.

then show that if one compensates a change of $a$ by an appropriate change of $R_{opt}$, the resulting curves are almost identical to the *standard* ones. It is therefore expected that the optical model analysis of the data contains an ambiguity between combinations of $R_{opt}$ and $a$. Indeed, we have obtained for each nucleus equivalent fits to the 179° excitation function for a whole family of combinations of $R_{opt}$ and $a$, some examples of which are shown in Fig. 4. Actually we observe here a remarkably stable linear relationship between ac-

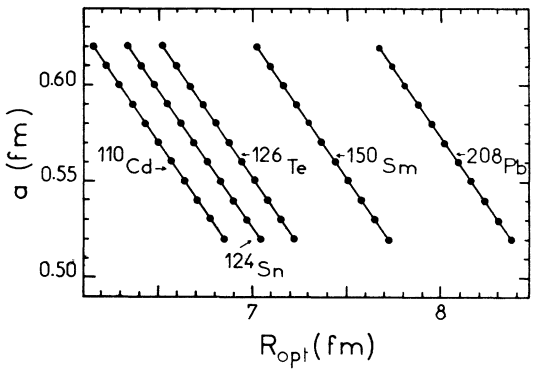


FIG. 4. Typical examples of combinations of $R_{opt}$ and $a$ which give equivalent fits, the parameters $V$ and $W$ being fixed to 200 and 20 MeV, respectively.

ceptable values of $R_{opt}$ and $a$, namely

$$R_{opt} + \alpha a \simeq R_0 . \tag{2}$$

Here $\alpha \simeq 7.0$ with slight variations from nucleus to nucleus, and the parameter $R_0$ is specific for each nucleus.

Relation (2) in a situation where the Igo relationship (1) holds can be expressed as

$$\mathrm{Re}U(R_0) \simeq -V \exp\left(\frac{R_{opt} - R_0}{a}\right)$$

$$= -V \exp(-\alpha) \simeq -0.2 \text{ MeV} . \tag{3}$$

This means that all Woods-Saxon potentials that fit the data have the same depth in the radial region around $R_0$. At first sight this seems to depend on our particular choice of $V = 200$ MeV. However, had we taken a different choice $V'$ for the real potential depth, this conclusion would have remained unchanged. Equation (2) could indeed have been replaced by

$$R'_{opt} + \alpha' a = R_0 \tag{4}$$

with the same $a$ and $R_0$, but, following the Igo relationship, with $R'_{opt} = R_{opt} + a \ln(V/V')$ and then $\alpha' = \alpha - \ln(V/V')$. We still would have

$$\mathrm{Re}U(R_0) = -V' \left[1 + \exp\left(\frac{R_0 - R'_{opt}}{a}\right)\right]^{-1}$$

$$\simeq -V' \exp(-\alpha') = -V \exp(-\alpha) \simeq -0.2 \text{ MeV} .$$

Here again it has been essential to make use of the condition

$$\exp\left(\frac{R_0 - R_{opt}}{a}\right) \gg 1 .$$

The choice of $V$ has therefore no effect on the interpretation of ambiguities (1) and (2). They express the fact that at *energies near the Coulomb barrier*, the $\alpha$-particle scattering data are fitted by any Woods-Saxon potential whose depth at $r = R_0$ is 0.2 MeV.

We can now summarize the relationships between $V$, $R_{opt}$, and $a$ in the simple equation

$$V \exp\left(\frac{R_{opt} - R_0}{a}\right) \simeq 0.2 \text{ MeV} \tag{5}$$

which expresses both above-mentioned ambiguities, Eqs. (1) and (2).

Figure 5 illustrates this situation by three numerically calculated examples. The tails of real nuclear potentials that fit $\alpha + \mathrm{Sn}$, $\alpha + \mathrm{Sm}$, and $\alpha + \mathrm{Pb}$ data are shown on a logarithmic scale. Each potential curve in this figure represents a whole potential family for a fixed parameter $a$, and where the parameters $R_{opt}$ and $V$ are connected by the Igo relationship. All potentials give equivalent fits to the 179° scattering cross sections. It is clearly

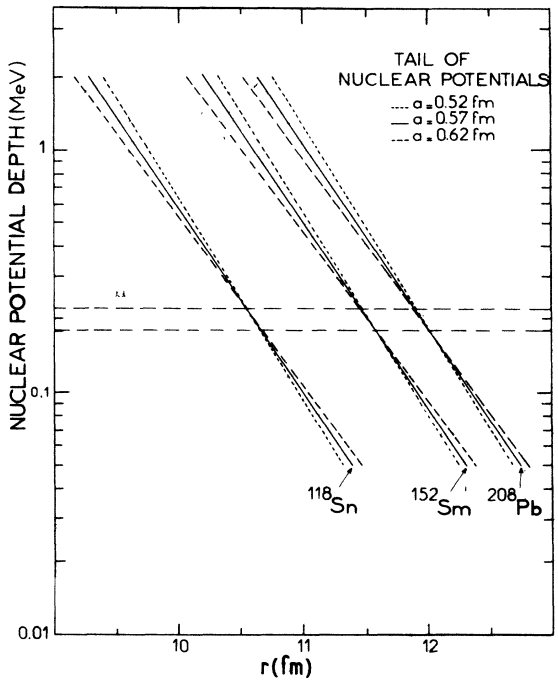


FIG. 5. Typical examples of Woods-Saxon potential tails for three values of the diffuseness $a$, namely, $a = 0.52$ fm, $a = 0.57$ fm, and $a = 0.62$ fm. Each line represents a whole family of Woods-Saxon potentials connected by the Igo relationship. For each nucleus, the tails cross in a narrow region where the potential depth is close to 0.2 MeV. The distance $R_{0.2}$ at which the potential depth is exactly 0.2 MeV is clearly determined without ambiguity for these Woods-Saxon potentials.

borne out that all real potentials that fit the data for one target nucleus have a common depth at $r = R_0$, namely, $V \exp(-\alpha)$.

However, since $\alpha$ is slightly different from one nucleus to the other the depth $V \exp(-\alpha)$ is not exactly 0.2 MeV but varies somewhat from nucleus to nucleus. It facilitates the comparison between nuclei (in the framework of the optical potential model we are using) to define a distance $R_{0.2}$ between the centers of target and projectile, by the requirement $U(R_{0.2}) = 0.2$ MeV. The values of $R_{0.2}$ will then be close to $R_0$ to the degree that Eq. (5) holds exactly. The quantity $R_{0.2}$ is extremely well defined in the framework of our parametrization of the scattering potential. Table II gives the values of $R_{0.2}$ for the 23 target nuclei investigated in our work.

We have made an attempt to determine the experimental uncertainty on each value of $R_{0.2}$, by using the fact that the theoretical curve is simply shifted towards higher or lower energies when $R_{0.2}$ is decreased or increased, respectively, while the slope of the exponential descent remains con-

stant. Therefore, a single experimental point in the descent of $\sigma/\sigma_R$ is sufficient, in principle, to determine $R_{0.2}$. We then have determined, for each nucleus, the value of $R_{0.2}$, independently for each point of the exponential decrease of $\sigma/\sigma_R$ and calculated the standard deviation from the *best fit* value

$$\Delta R = \left(\frac{1}{N}\sum_{i=1}^{N} \left| R_{0.2}^{(i)} - R_{0.2}^{(\text{best fit})} \right|^2\right)^{1/2}$$

The value of $\Delta R$ thus obtained appears in Table II.

We point out that the errors $\Delta R$ do not contain any contribution that would take into account the degree of arbitrariness in our parametrization of the potential.

The conclusion of the optical-model analysis is therefore:

(a) There is no sensitivity to the imaginary potential, provided its value is larger than about 10 MeV and smaller than about 40 MeV. Physically, this can be interpreted as follows: There is essentially no absorption of the $\alpha$-particle flux outside the barrier, and a total absorption once the barrier is surmounted.

(b) The only statement that can be made on the three parameters characterizing a Woods-Saxon real potential is that they are linked by the relationship

$$V \exp\left(\frac{R_{\text{opt}} - R_0}{a}\right) = \text{const} \simeq 0.2 \text{ MeV}.$$

Alternatively, we can define a new size parameter, namely, the distance $R_{0.2}$ where the real Woods-Saxon potential depth is 0.2 MeV, by the relationship

$$V \exp\left(\frac{R_{\text{opt}} - R_{0.2}}{a}\right) = 0.2 \text{ MeV}. \quad (6)$$

It is quite remarkable that at energies near the Coulomb barrier there exists a size parameter

TABLE II. Values of the $\alpha$-nucleus distance where the nuclear potential (of Woods-Saxon type) is 0.2 MeV deep. Our results are shown and compared with those of other authors. The $R_{0.2}$ values from Refs. 5–7 have been calculated from the potentials given by these authors.

| | | $R_{0.2}$ (fm) | | | |
|---|---|---|---|---|---|
| Nuclide | Present work | Goldring *et al.* (Ref. 5) | Eisen *et al.* (Ref. 6) | Tabor *et al.* (Ref. 7) | Werdecker (Ref. 9) |
| $^{110}$Cd | 10.44 ± 0.03 | | 11.48 | | 10.54 |
| $^{112}$Cd | 10.53 ± 0.03 | | 11.57 | | 10.54 |
| $^{114}$Cd | 10.61 ± 0.03 | | 10.60 | | 10.62 |
| $^{116}$Cd | 10.68 ± 0.03 | | 10.62 | | 10.62 |
| $^{112}$Sn | 10.42 ± 0.03 | | | | |
| $^{114}$Sn | 10.46 ± 0.02 | | | | |
| $^{116}$Sn | 10.53 ± 0.02 | | | 10.57 | |
| $^{118}$Sn | 10.59 ± 0.02 | | | 10.61 | |
| $^{120}$Sn | 10.63 ± 0.02 | | | 10.66 | |
| $^{122}$Sn | 10.66 ± 0.02 | | | 10.68 | |
| $^{124}$Sn | 10.79 ± 0.03 | | | 10.73 | |
| $^{122}$Te | 10.71 ± 0.03 | | | | |
| $^{124}$Te | 10.77 ± 0.03 | | 10.76 | | 10.76 |
| $^{126}$Te | 10.80 ± 0.03 | | 10.82 | | 10.80 |
| $^{128}$Te | 10.84 ± 0.03 | | 10.79 | | 10.81 |
| $^{130}$Te | 10.87 ± 0.03 | | | | |
| $^{142}$Nd | | | | 11.01 | |
| $^{144}$Nd | | | | 11.11 | |
| $^{146}$Nd | | | | 11.16 | |
| $^{148}$Nd | | | | 11.23 | |
| $^{150}$Nd | | | | 11.36 | |
| $^{144}$Sm | 11.04 ± 0.02 | | | | |
| $^{148}$Sm | 11.19 ± 0.03 | | | | |
| $^{150}$Sm | 11.31 ± 0.03 | | | | |
| $^{152}$Sm | 11.52 ± 0.07 | | | | |
| $^{204}$Pb | 11.92 ± 0.03 | 11.91 | | | |
| $^{206}$Pb | 11.91 ± 0.03 | 11.91 | | | |
| $^{208}$Pb | 11.97 ± 0.03 | 11.96 | | | |

which plays the role of the strong absorption radius at higher energies. This size parameter turns out be an $\alpha$-nucleus distance at which the real Woods-Saxon potential has a given value. This depth appears to increase with energy.[2,3] The average $A$ dependence of $R_{0.2}$ as found from a straight line least squares fit to all values of $R_{0.2}$ from Table II gives the following $A$ dependence

$$\bar{R}_{0.2} = (1.36A^{1/3} + 3.96)\ \text{fm}. \tag{7a}$$

If one takes into account only the nuclei known to be spherical, namely, the Sn and Pb isotopes and $^{144}$Sm, the straight line fit gives

$$\bar{R}_{0.2}^{(\text{sph})} = (1.355A^{1/3} + 3.93)\ \text{fm}. \tag{7b}$$

A quite interesting comparison can be made here with the recent work of Christensen and Winther.[9] These authors show that most heavy-ion elastic-scattering data can be fitted by a potential having an exponential tail of the form

$$\text{Re}U(r) = 50\frac{R_1R_2}{R_1+R_2}\exp\left(-\frac{r-R_1-R_2}{a}\right)\ \text{MeV}$$

with $R_i = 1.233A_i^{1/3} - 0.978A_i^{-1/3}$ fm and $a = 0.63$ fm. Values of $R_{0.2}$ deduced from such a potential fall on a straight line

$$R_{0.2}^{(\text{CW})} = 1.296A^{1/3} + 4.34$$

which is indeed very close to the average straight line fits to our data (7a) and (7b).

### B. Discussion: Is $R_{0.2}$ the best defined size parameter?

Goldring *et al.*[5] have measured elastic scattering of $\alpha$ particles at several angles and at energies close to the Coulomb barrier on $^{204,206,208}$Pb and $^{209}$Bi. As a result of their optical-model analysis, they define the *Rutherford radius* $R_R$ as the radius where the maximum of the Coulomb barrier is located, and consider $R_R$ as an interaction distance characteristic of the $\alpha$ scattering process and free of the optical-model parameter ambiguities. However, as is shown in Table III for the three lead isotopes, a variation of $a$ from 0.52 to 0.62 fm induces a variation of $R_R$ by 0.3 fm, and a variation of $V_B$, the potential at the top of the barrier, by 0.36 MeV. In contrast, values of $R_{0.2}$ change by at most 0.01 fm when $a$ varies from 0.52 to 0.62 fm. Furthermore, values of $R_{0.2}$ calculated from the set of parameters given by Goldring *et al.*[5] ($V = 100$ MeV, $W = 10$ MeV, $a = 0.58$ fm) agree with those calculated in this work within 0.01 fm. We then conclude that $R_{0.2}$ is a size parameter which is defined less ambiguously than $R_R$.

Werdecker[10] has measured $\alpha$ scattering at energies close to the Coulomb barrier on four Cd isotopes and three Te isotopes. He also uses the Rutherford radius $R_R$ as size parameter. Values of $R_{0.2}$ that we have deduced from the potentials that he has obtained are listed in Table II. The agreement is good except for $^{110}$Cd where the difference of 0.1 fm is 3 times our error bar of $\pm 0.03$ fm.

Other $\alpha$-particle scattering measurements at energies close to the Coulomb barrier have been performed on $^{110,112,114}$Cd and $^{128}$Te by Eisen *et al.*[6] These authors define an interaction radius on the basis of the incoming wave boundary method (IWB) as $R_E = R_R + 2.5a$, where $R_R$ is the Rutherford radius and $a$ is the same as our diffuseness parameter $a$. The nuclear potential at $R_E$ is close to

TABLE III. Dependence of the Rutherford radius $R_R$ on optical-model parameters. In the present work, values of $R_R$ and of the total potential at the barrier $V_B$ have been calculated by adjusting the optical-model radius for three values of the diffuseness $a$, and for $V = 200$ MeV and $W = 20$ MeV. Equivalent fits are then obtained. They are compared with the results of Goldring *et al.* (Ref. 5) obtained for $a = 0.58$ fm. Values of $R_R$ and $V_B$ are found to be much more sensitive to the diffuseness $a$ than $R_{0.2}$. A good agreement for all values is found for $a = 0.58$ fm.

| | | $R_R$ (fm) | | $R_{0.2}$ (fm) | | $V_B$ (MeV) | |
|---|---|---|---|---|---|---|---|
| Nuclide | $a$ (fm) | Ref. 5 | This work | Ref. 5 | This work | Ref. 5 | This work |
| $^{204}$Pb | 0.52 | | 11.09 | | 11.92 | | 20.31 |
| | 0.58 | 10.88 | 11.90 | 11.91 | 11.92 | 20.54 | 20.52 |
| | 0.62 | | 11.77 | | 11.91 | | 20.67 |
| $^{206}$Pb | 0.52 | | 11.08 | | 11.91 | | 20.33 |
| | 0.58 | 10.89 | 10.89 | 11.91 | 11.91 | 20.52 | 20.54 |
| | 0.62 | | 10.76 | | 11.90 | | 20.69 |
| $^{208}$Pb | 0.52 | | 11.14 | | 11.97 | | 20.21 |
| | 0.58 | 10.94 | 10.96 | 11.97 | 11.97 | 20.42 | 20.42 |
| | 0.62 | | 10.83 | | 11.96 | | 20.57 |

0.6 MeV. However, as we have shown above, an interaction radius such as $R_E$ depends on $a$ somewhat more than $R_{0.2}$. In Table II we have listed the values of $R_{0.2}$ that we have deduced from the parameters given by Eisen *et al.* The agreement with our results is very good.

Another $\alpha$-scattering experiment was performed by Tabor *et al.*[7] on the tin and neodymium isotopes. These authors have used a standard optical model to analyze their data, and conclude that they can deduce an interaction radius $R_{cf}$ which is very insensitive to variations of the optical-model parameters if they impose the condition that the *nuclear* potential at $R_{cf}$ be a *constant fraction* $\epsilon = 0.02$ of the *Coulomb* potential at $R_{cf}$. It appears that in the cases they have studied, the nuclear potential at $R_{cf}$ is 0.27 MeV. This value is rather close to the depth of 0.2 MeV which defines our interaction radius $R_{0.2}$. We find, however, that for mass 208, the radius at which the nuclear potential amounts to $0.02V_C = 0.4$ MeV is not determined with the same precision as $R_{0.2}$, since the curves in Fig. 5 corresponding to different values of $a$ intersect at a point where the depth is close to 0.2 MeV, a value which does not appear to vary with mass number. In Table II we have listed the values of $R_{0.2}$ that we have calculated from the potentials given by Tabor *et al.*[7] They agree quite closely with our results.

Finally, the $\alpha$ scattering on $^{152}$Sm has also been measured by Brückner *et al.*[11] They give elastic cross sections at 150 and 170° between 10 and 16 MeV. The comparison with the present results is difficult because of the coupled channel treatment that they have used to analyze their data.

The excellent agreement of the present results expressed by the values of $R_{0.2}$ with results of Refs. 5–7, 10, 11 shows that $R_{0.2}$ is indeed a good size parameter in a Woods-Saxon analysis of $\alpha$-particle scattering at energies close to the Coulomb barrier. Within this parametrization, it shows that the only statement that can be made on the usual Woods-Saxon parameters $V$, $R_{opt}$, and $a$ is contained in relation (6).

Finally, it is interesting to remark that this agreement has been obtained in spite of the fact that we have measured excitation functions at a single angle close to 180° while other authors[5,7,10,11] have measured excitation functions at several angles. This result seems to indicate that no additional information is gained by measuring the excitation functions at several angles. Figure 6 shows that indeed angular distributions calculated with different sets of parameters which give equivalent fits to the 180° excitation function yield almost identical angular distributions. Within the framework of such an optical-model analysis, it appears therefore that it is sufficient to measure excitation functions at a single large angle. Actually, the same information would probably be obtained by measuring a *single angular distribution* at a given energy 2 to 3 MeV above the Coulomb barrier.

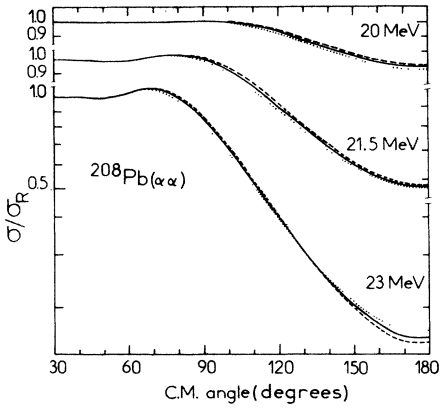


FIG. 6. Calculated angular distributions for the $^{208}$Pb case. The values of $V$ and $W$ have been kept fixed to 200 and 20 MeV, respectively. The full curves correspond to the *standard* values of $R_{opt}$ and $a$ as defined in Fig. 3, i.e., 8.03 and 0.57 fm, respectively. The dashed and dotted curves represent angular distributions obtained from the values of $R_{opt}$ and $a$ which give the same 180° excitation functions (Fig. 3). The dashed curve corresponds to $a = 0.52$ fm and $R_{opt} = 8.36$ fm while the dotted curve corresponds to $a = 0.62$ fm and $R_{opt} = 7.71$ fm.

## IV. ANALYSIS IN TERMS OF NUCLEON DENSITY DISTRIBUTIONS

### A. Summary of folding procedures

Bernstein,[12] Jackson and Kembhavi,[13] Morgan and Jackson,[14] and Budzanowski *et al.*[15] have shown that alpha-nucleus real potentials obtained in single or double folding procedures can give fits to the data as good as conventional Woods-Saxon potentials do. This approach is very similar to the one proposed by Slanina and McManus[16] and by Greenlees, Pyle, and Tang[17] for proton potentials. It has since been used by many authors. An extensive review of this subject has recently been given by Jackson.[18] Recent references can be found in the review papers of Rebel.[19]

This approach consists in using the multiple scattering expansion of Kerman, McManus, and Thaler,[20] and neglecting all terms in which intermediate states correspond to excited states of the nucleus.[13] The two-body interaction between the $\alpha$ particle and a target nucleon is then explicitly nonlocal, energy-dependent, and different from the free interaction. It is replaced by an *effective*,

local, energy-dependent interaction. The $\alpha$-nucleus potential is then

$$V_{opt}(R) = \lambda(E) \int \rho_N(r) V_{eff}(|\vec{r} - \vec{R}|) d^3r . \quad (8)$$

Here $\rho_N(r)$ stands for the radial nucleon distribution of the target nucleus, $V_{eff}(|\vec{r} - \vec{R}|)$ is the effective $\alpha$-nucleon interaction, $R$ being the coordinate of the $\alpha$-particle center of mass, and $\vec{r}$ being the coordinate of a nucleon in the target. The energy dependence of $V_{opt}(R)$ is explicitly given by $\lambda(E)$. Finally, $V_{eff}(|\vec{r} - \vec{R}|)$ is taken to be real, so that $V_{opt}(R)$ is the real part of the optical potential.

Tatischeff and Brissaud[21] have studied the behavior of $\lambda(E)$ at various energies and found that it decreases slowly with energy. For practical purposes, it is sufficient in the present case to incorporate $\lambda(E)$ into the normalization of the effective interaction. The role of exchange has been considered by Brissaud *et al.*[22] who used the pseudo-potential approach of Petrovich *et al.*[23] and Schaeffer.[24] They show that it modifies the $\alpha$-nucleus real potential in the interior but very little in the tail. We therefore ignore it in the present work.

The effective force $V_{eff}(r)$ is generally taken to be of Gaussian form

$$V_{eff}(r) = -U_0 \exp(-K^2 r^2) . \quad (9)$$

Jackson and Kembhavi[13] have shown that a Yukawa form yields potentials that are much too diffuse to allow good fits to the scattering data.

In a study of $\alpha$-particle scattering on $^{40}$Ca and $^{58}$Ni at 42 MeV, Batty, Friedman, and Jackson[25] have shown that equivalent results are obtained when $K$ takes values between 0.5 and 0.6 fm$^{-1}$, while $U_0$ is then fixed according to the relationship

$$U_0 K^{-6} = 2600 \text{ MeV fm}^6 . \quad (10)$$

This is in fair agreement with the values found by Bernstein[12] in his calculation of $V_{eff}$ from the matter distribution of the $\alpha$ particle and a phenomenological nucleon-nucleon interaction, namely, $U_0 = 37$ MeV, $K = 0.5$ fm$^{-1}$, giving $U_0 K^{-6} = 2368$ MeV fm$^6$. Morgan and Jackson[14] have found very similar values, $U_0 \simeq 36$ MeV and $K = 0.5$ fm$^{-1}$, from a fit to the $\alpha$-$^{40}$Ca and $\alpha$-$^{50}$Ti elastic scattering by a folding potential obtained with a fixed density distribution and a variety of $V_{eff}$.

A Woods-Saxon shape for $V_{eff}$ was, on the other hand, chosen by Mailandt, Lilley, and Greenlees[26] who deduced the parameters from an analysis of low-energy scattering of protons and neutrons off $^4$He. They give

$$V_{eff}(r) = -U_0 \left[1 + \exp\left(\frac{r - R_{eff}}{a_{eff}}\right)\right]^{-1} \quad (11)$$

with $U_0 = 42.5$ MeV, $R_{eff} = (2.35 - 0.0014E)$ fm, and $a_{eff} = 0.34$ fm, where $E$ is measured in units of MeV.

Finally, in a study of 42 MeV $\alpha$-particle scattering from nuclei ranging from $^{40}$Ca to $^{208}$Pb, Sumner[27] has determined an $\alpha$-nucleon effective interaction from the study of $\alpha$-particle scattering from $^{40}$Ca. For that purpose he used the density distribution of Negele[28] and determined which $\alpha$-nucleon effective forces reproduced the potential deduced from the analysis of his data. Negele's densities were chosen because: (a) they result from density-dependent Hartree-Fock calculations which should have the correct tail behavior and (b) Negele's proton density fits the best electron scattering data. The best choice of effective force from Sumner's work is then either a Gaussian force with $U_0 = 127$ MeV and $K = 0.6$ fm$^{-1}$ ($U_0 K^{-6} = 2722$ MeV fm$^6$) or, equivalently, a Woods-Saxon force with $U_0 = 42.5$ MeV, $R_{eff} = 2.35$ fm, and $a_{eff} = 0.35$ fm. It is quite remarkable that he obtains a result so close to the one of Mailandt *et al.*[26]

We have performed (1) a simplified analysis of our data by determining what a given value of $R_{0.2}$ for each nucleus implies for a Fermi-shaped nucleon density distribution and (2) a more complete analysis for two nuclei.

### B. Simplified analysis of the present data

Here we take the value of $R_{0.2}$ at its face value and neglect, in particular, its possible dependence on the detailed shape of the optical potential. Furthermore, we restrict ourselves to a Gaussian effective force with $U_0 = 127$ MeV and $K = 0.6$ fm$^{-1}$,[27] and to Fermi density distributions of the form

$$\rho_N(r) = \rho_0 \left[1 + \exp\left(\frac{r - C_N}{a_N}\right)\right]^{-1} . \quad (12)$$

This results in the following constraint on the nucleon density distribution $\rho_N(r)$

$$\int \rho_N(r)\{-U_0 \exp[-(K^2 |r - R_{0.2}|^2)]\} d^3r = -0.2 \text{ MeV} . \quad (13)$$

After integration over angles, this reduces to

$$\pi \frac{U_0}{K^2 R_{0.2}} \int_0^\infty \rho_N(r)\{\exp[-K^2(r - R_{0.2})^2] - \exp[-K^2(r + R_{0.2})^2]\} r\, dr = 0.2 \text{ MeV} . \quad (14a)$$

The central density $\rho_0$ should in principle be determined by the condition that

$$\int \rho_N(r)\, d^3r = A . \quad (15)$$

However, $R_{0.2}$ is always about 5 fm larger than the

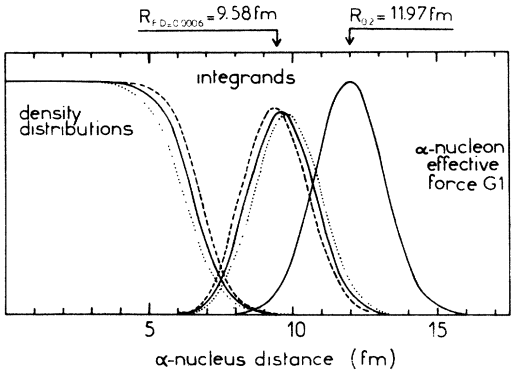


FIG. 7. Integrands of the folding integral (14a) are shown for $^{208}$Pb, along with the corresponding density distributions and the $\alpha$-nucleon effective force G1. The three density distributions shown yield the same nuclear potential of 0.2 MeV at $R_{0.2}=11.97$ fm. All three take the value $6\times10^{-4}$ nucleon/fm$^3$ at 9.58 fm. One can see that the integrands always have their maximum near $R_{\mathrm{FD}=0.0006}=9.58$ fm, and that in turn the folding integral (14 a) is sensitive to the value of the density in that region.

half-density radius $C_N$. Since the range ($\sim K^{-1}$) of $V_{eff}$ is about 2 fm, the integral in Eq. (14a) receives no appreciable contribution from radial regions with $r<C_N$ and is thus insensitive to the density distribution in the central region of the nucleus. This is illustrated by the examples given in Fig. 7 where the integrand of Eq. (14a) is shown as a function of $r$ for different values of the parameters $C_N$ and $a_N$ for which $\rho_N(r)$ satisfies Eq. (14a). Therefore the nucleon density $\rho_N$ needs to be defined only in the outer part of the nucleus. The normalization integral (15), on the contrary, depends so sensitively on the interior part of the nucleon density distribution that it is irrelevant in the present context. We have accordingly fixed $\rho_0$ at the reasonable value[29] of 0.16 nucleon/fm$^3$. We shall indeed show later on that the particular value of $\rho_0$ has actually no influence on the results of the analysis.

The parameters $U_0$, $K$, and $\rho_0$, now being fixed, Eq. (14) reduces to a relationship between $C_N$ and $a_N$. Actually this relationship is nearly linear in the range of $a_N=0.45$ fm to $a_N=0.60$ fm, which comprises generally accepted values. This relationship can therefore be approximately written as

$$C_N+\alpha_N a_N=C_0\,, \tag{14b}$$

where $\alpha_N=5.54\pm0.01$ for the nuclei under study. The nucleon density evaluated at $C_0$ is therefore

$$\rho_N(C_0)=\rho_0(1+\exp\alpha_N)^{-1}=6.3\times10^{-4}\ \text{nucleon/fm}^3$$

with small variations from nucleus to nucleus reflecting small variations of $\alpha_N$. At first glance this result seems to depend on the value of $\rho_0$. We have found, however, that for different values of $\rho_0$, the constant $\alpha_N$ determined in the way described above takes different values such as to keep $\rho_0/(1+\exp\alpha_N)$ constant. This can be qualitatively understood if we consider that the exponential tail $\rho_0\exp[(C_N-r)/a_N]$ of the nucleon density distribution $\rho_N(r)$ plays a dominant role in Eq. (14a). Indeed such a tail is not changed when $\rho_0$ is changed provided $a_N$ is kept fixed and $C_N$ is changed in such a way as to keep $\rho_0\exp(C_N/a_N)$ constant.

Since the values of $\rho_N(C_0)$ are slightly different for different nuclei, due to variations of $\alpha_N$, it is convenient to define for each nucleus a radius $R_{\mathrm{FD}=0.0006}$ (FD = fixed density) at which the density takes the value $6.10^{-4}$ nucleon/fm$^3$. This radius is close to $C_0$ and is then defined without ambiguity for any given choice of $C_N$ and $a_N$ within the framework of the present treatment. We have calculated $R_{\mathrm{FD}=0.0006}$ for all nuclei studied in this work. It turns out that the difference between $R_{0.2}$ and $R_{\mathrm{FD}=0.0006}$ is nearly constant

$$R_{\mathrm{FD}=0.0006}=R_{0.2}-(2.37\pm0.01)\ \text{fm}\,. \tag{16}$$

In other words, Eq. (14a) can approximately be written as

$$C_N+5.54a_N=R_{0.2}-2.37\ \text{fm}\,. \tag{14c}$$

### C. Detailed analysis of the $^{208}$Pb and $^{124}$Te nucleon distributions

The simplified analysis described above suffers from two drawbacks: (a) The value of $R_{0.2}$ may depend on the analytical form of the potential and therefore be different for a potential obtained by the folding method and (b) the results obtained may also depend on the analytical form of the nucleon density distribution and on the type of effective force that has been chosen. We have examined in detail these points for the case of $^{208}$Pb.

We have analyzed the $^{208}$Pb data by performing a complete optical-model calculation using real potentials obtained by the folding method. Two different types of nucleon density distributions and four different effective forces have been employed. The analytical forms of the nucleon density distributions were a Fermi-two-parameter form (F2)

$$\rho_N(r)=\frac{\rho_0}{1+\exp[(r-C_N)/a_N]}$$

or a modified Gaussian form (MG)

$$\rho_N(r)=\rho_0\frac{1+w(r^2/C_N{}^2)}{1+\exp[(r^2-C_N{}^2)/a_N{}^2]}\,.$$

The latter was used by Heisenberg *et al.*[30] in their analysis of $^{208}$Pb elastic electron scattering. We adopt their value of $w = 0.338$. In their analysis of 166 MeV $\alpha$ scattering from $^{208}$Pb, Tatischeff, Brissaud, and Bimbot[31] have also used this parametrization. We kept $\rho_0$ fixed to 0.16 nucleon/fm$^3$ for the reasons explained in Sec. IV B.

We have considered four different forces:

(1) Gaussian, with $U_0 = 127$ MeV, $K = 0.6$ fm$^{-1}$ (denoted G1),

(2) Gaussian, with $U_0 = 42.5$ MeV, $K = 0.5$ fm$^{-1}$ (denoted G2),

(3) Gaussian, with $U_0 = 37$ MeV, $K = 0.5$ fm$^{-1}$ (denoted G3),

(4) Woods-Saxon, with $U_0 = 42.5$, $R_{eff} = 2.35$ fm, $a_{eff} = 0.34$ fm (denoted WS).

The radial dependence of these forces is shown in Fig. 8. The two Gaussian forces G1 and G2 represent the two extremes among the Gaussian forces obeying the relation (10) of Batty *et al.*[25]

The Gaussian force G1 and the Woods-Saxon force WS are equivalent to the extent that for a given density distribution they give rise to potentials which differ by less than 1.5 keV outside the Coulomb barrier. In strong absorption situations, they ought to give identical scattering cross sections. This is actually confirmed in our optical-model calculations as was the case in the work of Sumner.[27]

We have then performed optical-model calculations with the density distribution F2 for $a_N = 0.45$ to 0.60 fm in steps of 0.15 fm for the three forces G1, G2, and G3. Actually, force G3 gives results which are intermediate between those of G1 and G2, and are in fact closer to those of G2. We found it therefore sufficient to restrict the calculations with density distributions MG to forces G1 and G2. In the case of density distributions MG, calculations were done for $a_N = 2.7$ to 3.1 fm, in steps of 0.1 fm. In all cases a value of $C_N$ was found which gave a satisfactory fit to the data.

In all these optical-model calculations, we have used a Woods-Saxon imaginary potential with a radius $R_W = 8.03$ fm and a diffuseness $a_W = 0.57$ fm. These values correspond to actual results of the phenomenological analysis of Sec. III. However, real potentials obtained by the folding method may have central depths of 400 to 500 MeV. We had, therefore, to increase the central depth of the imaginary potential to 25 to 40 MeV in order to maintain a total absorption of the $\alpha$-particle flux inside the nucleus, since this absorption is at each point proportional to $W(r)$ and to the reciprocal of the particle velocity.[32]

The results of all optical-model calculations appear in Figs. 9 to 12. In Fig. 9 the tails of nuclear potentials corresponding to the different combinations described above are shown. It is seen that for each combination of density and force the results are fairly insensitive to the precise value of $a_N$. However, all tails corresponding to different values of $a_N$ cross in a narrow region. The position of this crossing region appears to depend very little on the analytical form of the density distribution. In contrast, the variation of the range of the force (from G1 to G2) has a stronger effect. These results are summarized in Fig. 10 where the hatched area comprises all tails of the potentials of Fig. 9. Also shown in Fig. 10 are the Woods-Saxon potentials corresponding to values of $a$ of 0.52 and 0.62 fm, respectively. From this we conclude that, although the value of the potential of 0.2 MeV at $R_{0.2} = 11.97$ fm lies within the hatched area, the $\alpha$-nucleus distance $R_{0.2}$ is not as precisely given as in the Woods-Saxon analysis. On the other hand, the $\alpha$-nucleus distance at which the potential is 0.5 to 0.6 MeV deep is fairly well de-

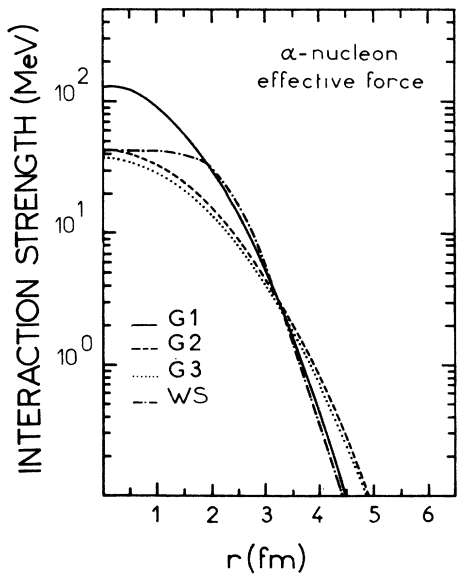


FIG. 8. Radial dependence of the $\alpha$-nucleon effective forces used in the $^{208}$Pb$(\alpha\alpha)$ analysis. G1, G2, and G3 are Gaussian shaped, with central strength of 127, 42.5, and 37 MeV, respectively, and range parameter $K$ of 0.6, 0.5, and 0.5 fm$^{-1}$, respectively. WS is the Woods-Saxon force $-U_0 \times \{1+\exp[(r-R_{eff})/a_{eff}]\}^{-1}$, with $U_0 = 42.5$ MeV, $R_{eff} = 2.35$ fm and $a_{eff} = 0.34$ fm.

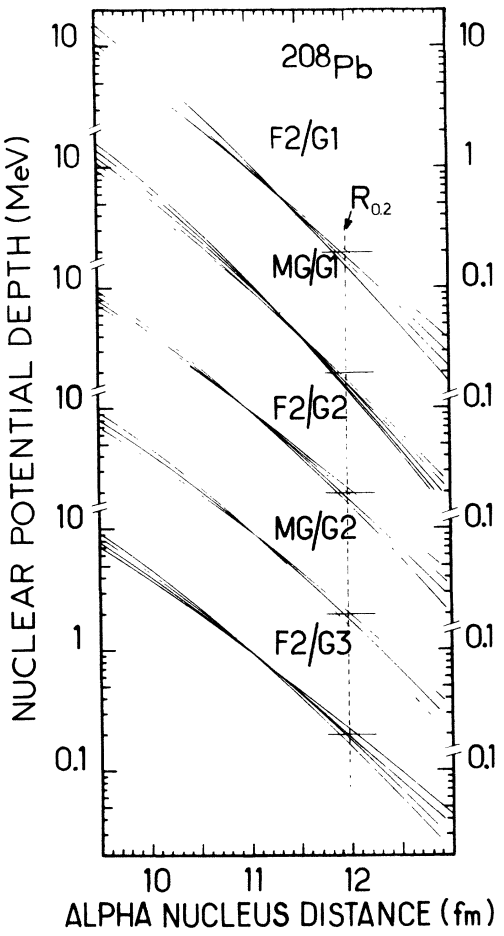


FIG. 9. Tails of nuclear potentials giving equivalent fits to the $^{208}$Pb data and which are obtained by folding several effective forces into various density distributions. Five combinations of density distributions (F2 or MG) and effective forces (G1, G2, G3) are shown. In each case, the value of the radius parameter $C_N$ has been adjusted for values of $a_N$ ranging from 0.45 to 0.60 fm in 0.15 fm steps (F2 densities) or 2.7 to 3.1 fm in 0.1 fm steps (MG densities). The value of $R_{0.2}$ of 11.97 fm obtained in the Woods-Saxon analysis is shown for comparison.

termined. For example, the distance at which the nuclear potential is 0.5 MeV is 11.45 fm ± 0.05 fm if we take into account all potentials that we have considered in the present section as well as the Woods-Saxon potentials discussed in Sec. III.

Likewise, the nucleon density distributions from which these potentials have been calculated are shown in Fig. 11. Here again, there is a fairly well determined crossing region for all curves corresponding, for different values of $a_N$, to a given combination of effective force and density distribution. The location of this crossing region depends much more strongly on the choice of the

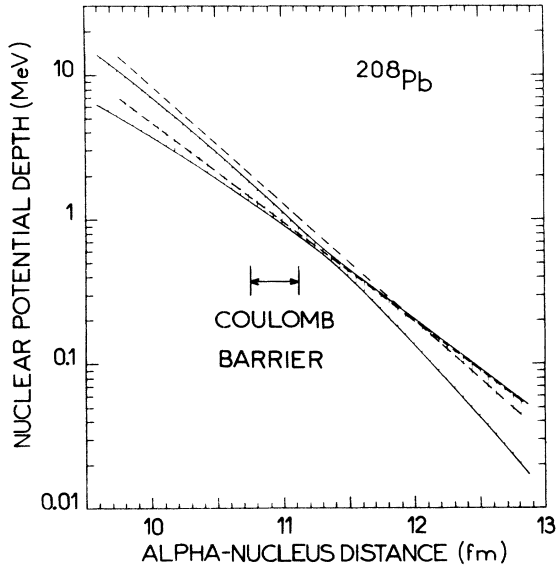


FIG. 10. Limits to the $\alpha$-$^{208}$Pb nuclear potential tails. All tails shown in Fig. 8 lie within the hatched area. The maximum of the Coulomb barrier lies between the two arrows for the cases shown in Fig. 8. The two dashed curves represent the two extreme potentials obtained in the Woods-Saxon analysis. They correspond to diffuseness parameters $a$ of 0.52 and 0.62 fm, respectively.

force than on the analytical form of the density distribution. Figure 12 summarizes the results concerning the tail of the nucleon density distribution of $^{208}$Pb. The hatched area comprises all such distributions for which $0.50 \leq a_N \leq 0.55$ (F2 distributions) or $2.8 \leq a_N \leq 3.0$ (MG distributions). Those distributions for which $0.45 \leq a_N \leq 0.60$ (F2) or $2.7 \leq a_N \leq 3.1$ (MG) are comprised between the dashed curves.

The hatched area as well as the area between the two dashed curves show a necking at density values aroung $2 \times 10^{-3}$ nucleon/fm$^3$ so that we can define a *fixed-density radius* $R_{FD=0.002}$ where the nucleon density takes the value of $2 \times 10^{-3}$ nucleon/fm$^3$. For $^{208}$Pb, we have

$$R_{FD=0.002} = 8.86 \pm 0.14 \text{ fm}. \quad (17)$$

The uncertainty of ±0.14 fm that we assign here is half the distance between the two dashed curves of Fig. 12 at the density of $2 \times 10^{-3}$ nucleon/fm$^3$. We consider it as a measure of the model-dependent uncertainty on $R_{FD}$ (in the following we will use $R_{FD}$ for $R_{FD=0.002}$). Figure 12 shows that this uncertainty is due to the uncertainty on the range of the effective force rather than to the uncertainty on the slope parameter $a_N$.

We have performed the same analysis for the $^{124}$Te data and have found potentials and density distributions identical to those of $^{208}$Pb, except

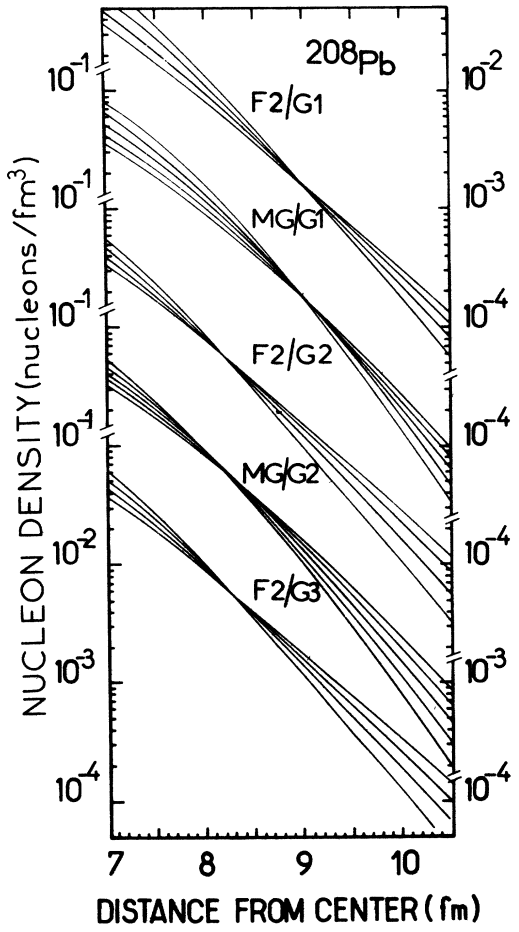


FIG. 11. Tails of the nucleon density distributions corresponding to the potentials of Fig. 8. Each curve represents a density obtained by adjusting the radius $C_N$ for a set of values of $a_N$ (0.45 to 0.60 fm in steps of 0.15 fm for $F2$ densities and 2.7 to 3.1 fm in steps of 0.1 fm for MG densities).

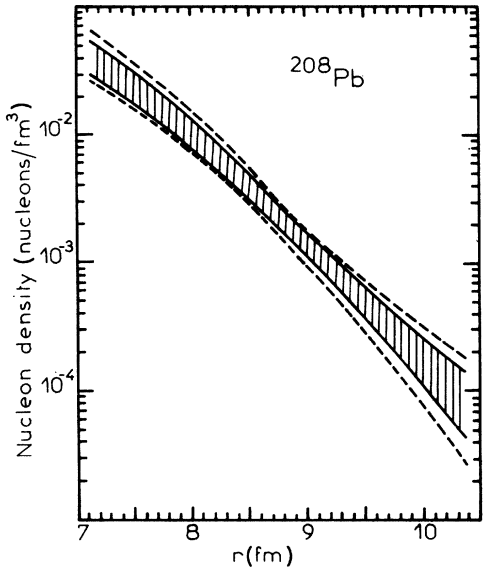


FIG. 12. Limits to the tail of the $^{208}$Pb nucleon density distribution. All densities of Fig. 11 lie between the two dashed curves. Densities restricted to $0.50 \leq a_N \leq 0.55$ ($F2$ densities) or $2.8 \leq a_N \leq 3.0$ (MG densities) lie within the hatched area. It is clear that the main cause of uncertainty comes from the uncertainty on the range of the effective force since the hatched area is only slightly narrower in the *neck* than the area between the two dashed curves.

for a shift of 1.20 fm towards smaller radii. This holds for each individual curve in Figs. 9 and 11, and in particular for $R_{FD}$. The 1.20 fm difference between the two $R_{FD}$'s is exactly equal to the difference between the $R_{0.2}$ values of $^{124}$Te and $^{208}$Pb.

In other words, we have

$$R_{0.2}(^{124}\text{Te}) - R_{FD}(^{124}\text{Te}) = R_{0.2}(^{208}\text{Pb}) - R_{FD}(^{208}\text{Pb}) = (3.11 \pm 0.14)\ \text{fm}.$$

Indeed such a result is not surprising if we consider that: (i) the nuclei considered here have $A \geq 110$ and have therefore a radius which is large compared to their surface thickness, (ii) the data are sensitive only to the surface region of the density distribution (Fig. 7).

It is then fair to assume that in general we have for all nuclei considered in this paper

$$R_{FD} = R_{0.2} - (3.11 \pm 0.14)\ \text{fm}. \quad (18a)$$

### D. Present data and the choice of the effective force

It is interesting to note that among the density distributions that were used here (Fig. 11), two are very close to the Negele calculation[28] in the radial region of 7 to 10 fm. One is of F2 type with $a = 0.55$ fm and the other one is of MG type with $a = 3.0$ fm. Both give good fits to the data in conjunction with force G1. Had we used Negele's density distribution to determine the effective force, we would find a force identical to the ones of Sumner[27] (G1) or Mailandt *et al.*[26] since the latter is very close to WS, which was found to be strictly equivalent to G1. *A priori*, there is no strong reason why Negele's calculations, which give equally good results on the charge distributions of $^{40}$Ca and $^{208}$Pb would give a poorer neutron distribution for $^{208}$Pb than for $^{40}$Ca. We have, moreover, two evidences that they are equally good: (i) the density distributions obtained by Sumner with a G1 force fit equally well the Negele calculations of $^{40}$Ca and $^{208}$Pb; (ii) Negele's density distribution of $^{208}$Pb is in very close agreement with a quite different calculation made by Royer, Dost,

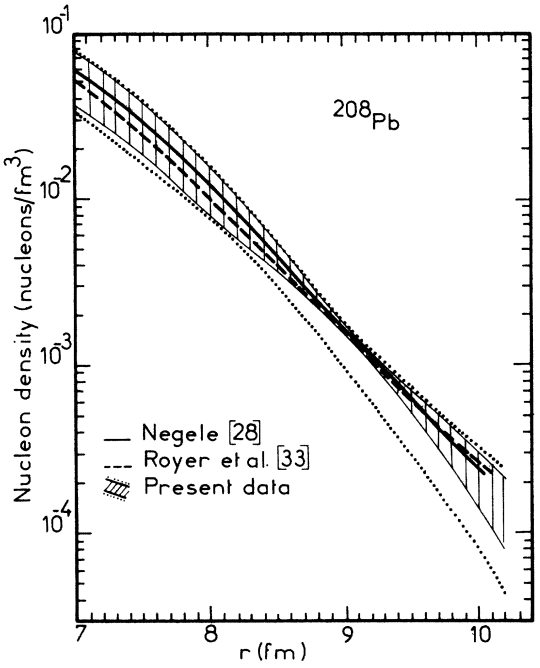


FIG. 13. Tails of density distributions of $^{208}$Pb. Calculations of Negele (Ref. 28) and Royer *et al.* (Ref. 33) are compared with the present work. The hatched area comprises all $^{208}$Pb densities compatible with the present data and the effective force G1. All densities compatible with the present data and all forces shown in Fig. 8 lie between the two dotted curves.

and Doubre.[33] These authors have calculated a nucleon density distribution for $^{208}$Pb from a shell model potential which they fitted to both the nucleon separation energies and nucleon transfer cross sections in the neighborhood of $^{208}$Pb. The density distribution is then calculated by summing over the squared wave functions of all occupied shell model orbits. It depends mainly on the nuclear interior (through the nucleon separation energies) and the surface region in the vicinity of $\simeq$10 fm (through the nucleon transfer cross sections). The tails of these two calculated density distributions are shown in Fig. 13. We therefore consider that there is a definite evidence in favor of an effective force of type G1, namely, a Gaussian force with $U_0 = 127$ MeV and $K = 0.6$ fm$^{-1}$. Moreover, at the very low densities considered here, the *effective* $\alpha$-nucleon interaction is expected to be close to the *free* one. This is indeed so for G1, which was found to be equivalent to WS. The WS force is in fact the low-energy limit of the $\alpha$-nucleon interaction of Maillandt *et al.*,[26] who deduced it from an analysis of free proton-$\alpha$ and neutron-$\alpha$ low-energy scattering.

If this effective force is used, the density distributions which are compatible with the present data lie in the hatched area of Fig. 13. It is clear that the value of $R_{FD}$ is then defined more precisely; now we have

$$R_{FD}(^{208}\text{Pb}) = (8.91 \pm 0.03)\ \text{fm}$$

and more generally

$$R_{FD} = R_{0.2} - (3.06 \pm 0.03)\ \text{fm}. \qquad (18b)$$

We therefore conclude that the value of $R_{FD}$ is very probably given by (18b) although the larger spread of (18a) cannot be excluded.

Finally we note that the result of the simplified analysis [Eq. (16)] described in Sec. IV B and which gave within ±0.01 fm the radius at which the density is $6 \times 10^{-4}$ nucleon/fm$^3$ was too optimistic. Indeed Fig. 13 shows that this radius can only be determined within ±0.1 fm if the choice of the effective interaction is limited to G1, and to ±0.23 fm if interactions G1 and G2 are considered.

### E. Variation of the nucleon fixed-density radius $R_{FD=0.002}$ with mass number

Figure 14 shows the variation as a function of $A^{1/3}$ of $R_{FD}$ that we have defined in the preceding section as the radius at which the nucleon density equals $2 \times 10^{-3}$ nucleon/fm$^3$. The full curve represents a straight line fit through the $R_{FD}$ values

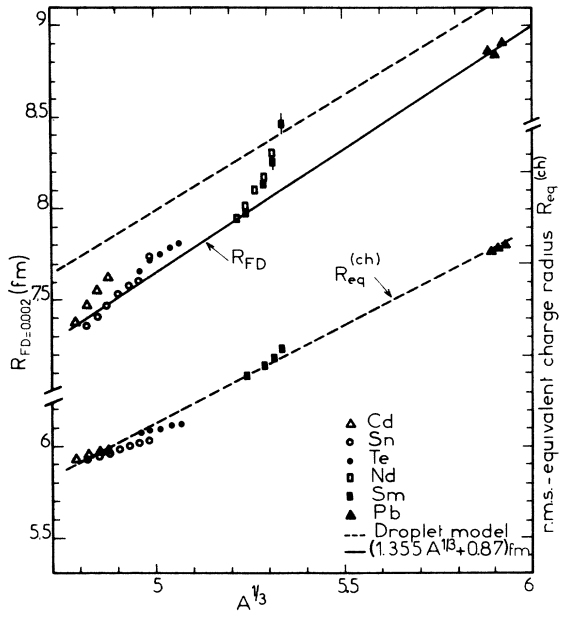


FIG. 14. Variation of $R_{FD}$ as a function of $A^{1/3}$. Also shown are the values of the rms equivalent charge radius $R_{eq}^{(ch)}$ deduced from the literature (see text). The full curve is a straight line least squares fit to $R_{FD}$ values of spherical nuclei. The two dashed curves are straight line fits to the predictions of the droplet model for $R_{eq}^{(ch)}$ and $R_{FD}$.

of nuclei known to be spherical (Sn and Pb isotopes, $^{144}$Sm):

$$\langle R_{FD}^{(sph)}\rangle = (1.355A^{1/3} + 0.87)\ \text{fm}. \quad (19a)$$

A similar fit to all $R_{FD}$ values gives a rather similar result:

$$\langle R_{FD}\rangle = (1.361A^{1/3} + 0.90)\ \text{fm}. \quad (19b)$$

This result is, however, of lesser significance because of the influence of $R_{FD}$ values of deformed nuclei which strongly differ from the average behavior.

In Fig. 14 are also plotted the values of the rms equivalent radii of charge distributions that can be found in the literature. We have used the results of Ficenec *et al.*[34] for Sn isotopes, of Heisenberg *et al.*[30] for $^{208}$Pb, and of Cardman *et al.*[35] for $^{148}$Sm. The rms-equivalent charge radii $R_{eq}$ of $^{204,206}$Pb and $^{144,150,152}$Sm were calculated from the isotope-shift measurements of Lee and Boehm.[36] For Cd and Te isotopes, we have used the muonic-atom measurements of Backenstoss and Goebbel[37] on natural targets and calculated the variations within each series of isotopes from isotope-shift measurements.[38] A straight line fit through the points gives for the average $\langle R_{eq}\rangle$:

$$\langle R_{eq}\rangle = (1.107A^{1/3} + 0.565)\ \text{fm}. \quad (20)$$

In order to discuss the difference in the slopes of $\langle R_{FD}\rangle$ and $\langle R_{eq}\rangle$, we find it convenient to compare each of them to the values given by the *droplet model*.[39] This is an extension of the *liquid drop model* where the surface is no longer required to be sharp, and the nuclear compressibility is allowed to have a finite rather than infinite value. We have used the Fermi-type approximations to the droplet-model densities of spherical nuclei as given by Myers,[40] to calculate $R_{FD}^{(DM)}$ values, although this extrapolation of the droplet model is not expected to be valid at densities as small as $2\times10^{-3}$ nucleon/fm$^3$. However, since the same surface diffuseness of 0.55 fm is used for all nuclei, the variation of $R_{FD}^{(DM)}$ with mass number is parallel to that of the half-density radius. Droplet-model values of the rms-equivalent charge radius $R_{eq}^{(DM)}$ have been calculated as well (and corrected for nucleon size). Straight line fits to these values give

$$\langle R_{eq}^{(DM)}\rangle = (1.081A^{1/3} + 0.72)\ \text{fm} \quad (21)$$

and

$$\langle R_{FD}^{(DM)}\rangle = (1.248A^{1/3} + 1.72)\ \text{fm}. \quad (22)$$

One can observe a nearly perfect agreement between the droplet-model and the observed rms-equivalent charge radii. As for $R_{FD}$, the droplet model gives *absolute values* which are 0.32 fm (Sn region) to 0.22 fm (Pb region) too high, a quite good result indeed. Considering the *slope* of $R_{FD}$ versus $A^{1/3}$, the droplet model gives a value which is 0.107 fm amu$^{-1/3}$ too small, which corresponds to a variation of $-0.12$ fm from $^{112}$Sn to $^{208}$Pb, of the difference between our value of $R_{FD}$ and the one calculated in the droplet model. To the extent that the droplet model described correctly the average "bulk" properties of nuclei (like in particular $R_{eq}^{(ch)}$), we have here a good evidence that *the surface thickness of spherical nuclei does not vary appreciably in the region* $112 \leq A \leq 208$.

As can be recognized from Fig. 14, the slope of $R_{FD}$ versus $A^{1/3}$ within each series of isotopes differs in most cases from the average value of 1.361 fm amu$^{-1/3}$. We note that the cadmium radii $R_{FD}$ follow a slope of 2.8 fm amu$^{-1/3}$, a fact that appears to point to the "soft" character of cadmium isotopes. A more pronounced case is that of the samarium isotopes, where the slope of $R_{FD}$ is 4.8 fm amu$^{-1/3}$.

$R_{FD}$ values deduced from the results of Tabor *et al.*[7] on Nd isotopes are also shown in Fig. 14. It is remarkable that the variation of $R_{FD}$ with increasing number of neutrons is very parallel in Sm and Nd isotopes. Tabor *et al.* have shown that the large variations of radii which are observed can be accounted for by taking explicitly into account the deformation of these nuclei in a coupled channel calculation. This holds probably for the Sm isotopes as well.

## V. DISCUSSION: COMPARISON OF PRESENT RESULTS TO EXPERIMENTAL INFORMATION ON THE NUCLEON DENSITY IN THE REGION AROUND $R_{FD}$

### A. Comparison of the present values of $R_{FD}$ to the results of $K^-$ absorption by heavy nuclei

A number of authors have tried to relate experimental information on $K^-$ capture in the nuclear periphery to the extension of matter density into regions far beyond the half-density radius. Burhop[41] and Burhop *et al.*[42] have interpreted the experiment of Davis *et al.*[43] on $K^-$ capture in emulsion nuclei and concluded that in the radial region of Ag where the capture occurs, the ratio $\rho_n/\rho_p$ of neutron and proton densities is higher than $N/Z$. Ericson and Scheck[44] concluded, on the contrary, that $K^-$ absorption from $K^-$ atomic orbits, as borne out by the cutoff in the x-ray cascade,[45] is consistent with $\rho_n^{(r)}/\rho_p^{(r)} = N/Z$ at *all* radii out to the capture region. This region extends over several fm, but the maximum $K^-$ capture probability occurs in the heaviest nuclei at about 2 fm beyond the nuclear half-density radius, i.e., only slightly inside our fixed-density radius $R_{FD}$.[46,47]

It is therefore quite interesting to compare these

results to ours, which can be done for $^{208}$Pb. In Fig. 15 the hatched area comprises all tails of nucleon density distributions compatible with our data, as was discussed in Secs. IV C and IV D. On the same figure are shown the tails of density distributions found to be compatible with $K^-$ absorption data[43] by Bethe and Siemens[46] and Ericson and Scheck.[44]

### B. Relation to other types of information on the nuclear density distribution

We are now going to attempt to relate the present results to other existing information on the density distributions. It should be noted, however, that in some cases such comparisons can only be made in an indirect way, by means of some extrapolation, which introduces a certain arbitrariness. We shall consider the following types of experimental information:

#### *1. Comparison to charge distributions*

It is interesting to compare the present data to charge distribution data and see if they show any evidence for a neutron halo in neutron-rich nuclei. For that purpose we have used the charge distributions determined from electron scattering measurements for tin isotopes[34] and for $^{208}$Pb.[30] Proton densities (corrected for proton size) calculated for these nuclei at $R_{FD}$ are shown in Table IV. Also shown in Table IV are the values of the total density at $R_{FD}$ that one finds by multiplying the proton density by $(N+Z)/Z$, i.e., assuming the same radial distribution (and hence same rms radius) for protons and neutrons, with densities in the ratio $Z/N$ at all radii. The estimated error on our $R_{FD}$ values [Eq. (18b)] can be expressed

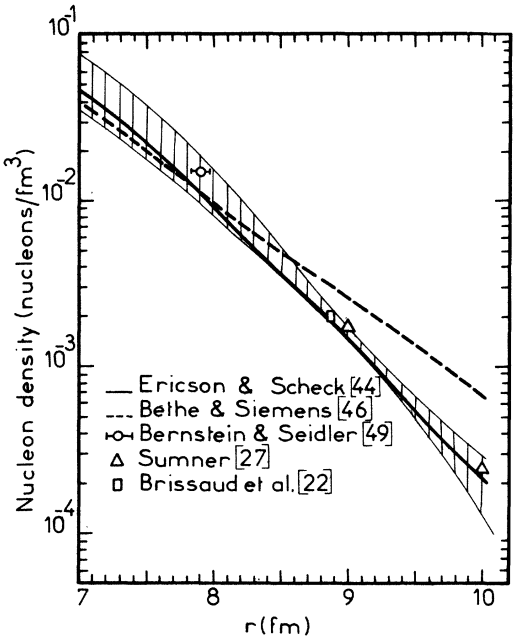


FIG. 15. Comparison between the present analysis which restricts the nucleon density distribution of $^{208}$Pb to the hatched area and various other results (see text).

in terms of an uncertainty on the density at $R_{FD}$, which is then $(2.0 \pm 0.1) \times 10^{-3}$ nucleon/fm$^3$ without excluding a larger spread of $(2.1 \pm 0.6) \times 10^{-3}$ nucleon/fm$^3$ [corresponding to Eq. 18(a)]. The statistical error of ±0.03 fm gives in addition an uncertainty of ±0.1 nucleon/fm$^3$. Table IV then shows that, except for the most neutron-rich nuclei, absolute values of the densities estimated from electron scattering data are higher than our results, especially if we consider that the neutron-to-pro-

TABLE IV. Proton densities calculated at $R_{FD}$ from charge distributions given by Ficenec *et al.* (Ref. 34) for tin isotopes and Heisenberg *et al.* (Ref. 30) for $^{208}$Pb. Corrections for finite proton size have been included. In column 3 are shown the total nucleon densities that are deduced from the proton densities by assuming the same radial shape for both types of nucleons.

| Nuclide | $R_{FD}$ (Present work) (fm) | $\rho_p(R_{FD}) \times 10^3$ (protons/fm$^3$) | $\frac{N+Z}{Z}\rho_p(R_{FD}) \times 10^3$ (nucleons/fm$^3$) |
|---|---|---|---|
| $^{112}$Sn | 7.36 | 1.39 | 3.11 |
| $^{114}$Sn | 7.40 | 1.32 | 3.01 |
| $^{116}$Sn | 7.45 | 1.13 | 2.62 |
| $^{118}$Sn | 7.53 | 1.02 | 2.41 |
| $^{120}$Sn | 7.57 | 0.93 | 2.23 |
| $^{122}$Sn | 7.60 | 0.89 | 2.17 |
| $^{124}$Sn | 7.73 | 0.67 | 1.66 |
| $^{208}$Pb | 8.91 | 0.70 | 1.78 |

ton ratio at $R_{FD}$ is probably higher than $N/Z$. This discrepancy can be due to the fact that charge distributions extrapolated to these large distances may be rather uncertain, as model-independent analyses of electron scattering data have shown.[48] It can be noted, however, that the proton density at $R_{FD}$ decreases monotonically with increasing neutron number in the tin isotopes, and takes almost the same value for $^{124}$Sn and $^{208}$Pb which have nearly equal $N/Z$ ratios (1.48 and 1.54, respectively). Moreover, the error on the *variation* of $R_{FD}$ is closer to that of $R_{0.2}$, i.e., ±0.03 fm. There is therefore an evidence that the neutron-to-proton density ratio at $R_{FD}$ is increasing faster than $N/Z$.

### 2. Comparison to α-particle scattering at energies between 42 and 104 MeV

These experiments are sensitive to not quite as remote a region of the surface of the nucleon density distribution. Bernstein and Seidler[49] have analyzed the 104 MeV data of Hauser *et al.*[50] using Fermi nucleon densities and the effective force G3. They have shown that the nucleon density is best known at a distance $\bar{r} \equiv R_{FD=0.015}$ where it takes the value $\rho_N(\bar{r}) = 1.5 \times 10^{-2}$ nucleon/fm$^3$. In the case of $^{208}$Pb, they find $R_{FD=0.015} = 7.90 \pm 0.06$ fm, in excellent agreement with our data (see Fig. 15).

Sumner[27] has used a Woods-Saxon optical model to analyze 42 MeV data on a range of nuclei. He used the effective force G1 to unfold the tail of the real part of the potential, thus obtaining the tail of a nucleon density which fits his data. We can compare his results to ours for $^{118}$Sn and $^{208}$Pb. For $^{118}$Sn, he finds a nucleon density of $2 \times 10^{-3}$ nucleon/fm$^3$ at 7.65 fm. However, along the lines of our discussion in Secs. IV C and IV D, the present data give for $^{118}$Sn a very probable value of $R_{FD} = 7.53 \pm 0.03$ fm (with a statistical error of ±0.02 fm) without excluding values as high as 7.62 fm. Thus we do not have here a real disagreement. As for $^{208}$Pb, Sumner finds $\rho_N(r = 9\text{ fm}) = 1.75 \times 10^{-3}$ nucleon/fm$^3$ and $\rho_N(r = 10\text{ fm}) = 2.4 \times 10^{-4}$ nucleon/fm$^3$, in excellent agreement with our results (Fig. 15).

### 3. Comparison to $\rho^0$-meson photoproduction

Experiments of $\rho^0$-meson photoproduction on nuclei have been given an interesting interpretation by Alvensleben *et al.*[51] in terms of strong interaction radii. They can explain their results in terms of a Fermi-type matter density distribution having a surface diffuseness $a = 0.545$ fm and a half-density radius compatible with $R(A) = (1.12 \pm 0.02)A^{1/3}$ fm. The most sensitive radial region in these experiments is close to the half-density radius. Yet the data are compatible with variations of ±10% of the diffuseness parameter $a$. They obtain for $^{208}$Pb $R(A) = 6.82 \pm 0.20$ fm and for a natural cadmium target $R(A) = 5.40 \pm 0.14$ fm. We have calculated for these two cases the radii $R^{ALV}_{FD=0.002}$ at which the density is $2 \times 10^{-3}$ nucleon/fm$^3$ for values of $a$ ranging from 0.5 to 0.6 fm. For $^{208}$Pb, we find for $R^{ALV}_{FD=0.002}$ values between 8.97 and 9.38 fm to be compared with our value of 8.91 ± 0.03 fm, while for Cd we find for $R^{ALV}_{FD=0.002}$ values between 7.58 and 7.99 fm, to be compared with our average value of 7.44 ± 0.11 fm. These values are not in real disagreement, although our values seem to be lower than those of Alvensleben *et al.* Indeed this should be considered as a good agreement in view of the fact that the two measurements test a different radial region of the density distribution and depend on completely different elementary interaction cross sections. Furthermore, the $\rho_0$-photoproduction experiment was done with targets of natural isotope composition, which makes the comparison with our data somewhat involved for the Cd case.

### 4. Comparison to experiments sensitive to the rms radius of the nucleon density distribution

Brissaud *et al.*[22] have measured α-particle scattering at 166 MeV on a range of nuclei. They ob-

TABLE V. Root-mean square radii of density distributions from Refs. 22, 17, and 52 (columns 3 to 5). Comparison to the present work is made by calculating $R_{FD=0.002}$ values from the densities of Ref. 22.

| | $R_{FD=0.002}$ (fm) | | rms radius (fm) | | |
|---|---|---|---|---|---|
| Nuclide | Present work | Brissaud *et al.* (Ref. 22) | Brissaud *et al.* (Ref. 22) | Greenlees *et al.* (Ref. 17) | Boyd *et al.* (Ref. 52) |
| $^{116}$Sn | 7.47 | 7.59 | 4.58 ± 0.05 | | 4.77 ± 0.10 |
| $^{118}$Sn | 7.53 | 7.81 | 4.65 ± 0.05 | | 4.77 ± 0.10 |
| $^{120}$Sn | 7.57 | 7.85 | 4.70 ± 0.05 | 4.66 ± 0.11 | 4.87 ± 0.10 |
| $^{124}$Sn | 7.60 | 7.72 | 4.68 ± 0.05 | | 4.96 ± 0.10 |
| $^{208}$Pb | 8.91 | 8.87 | 5.59 ± 0.05 | 5.52 ± 0.15 | |

tained good fits to their data by folding the effective force G3 into a density distribution of the following form. They have taken a proton distribution from the literature[30] and used the same distribution for neutrons, except that they allowed the radius parameter $C_N$ to vary. Their analysis shows that their data are most sensitive to the radial region of the density distribution close to its rms radius. In Table V we compare their results to ours for some Sn isotopes and for $^{208}$Pb. In the first two columns, $R_{FD}$ values calculated for the density distributions of Brissaud *et al.* are compared to our results. While the agreement is perfect for $^{208}$Pb, Brissaud's values for Sn isotopes are 0.2 to 0.3 fm higher than ours. In view of the fact that the two experiments test completely different radial regions of the density distribution, this agreement is quite satisfactory, and hence the rms radii of Brissaud *et al.* are compatible with our results.

Proton scattering at various energies has been shown to be sensitive to the rms radius of the nucleon distribution.[17] In particular Boyd *et al.*[52] have given rms radii for some Sn isotopes and Greenlees *et al.*[17] for $^{120}$Sn and $^{208}$Pb. These results appear in Table V. To the extent that Greenlees's results agree with those of Brissaud *et al.*, they are compatible with the present work. The rms radii of Boyd *et al.*[52] are 0.1 to 0.3 fm higher than those of Brissaud *et al.*[22] In view of the fact that Brissaud's values of $R_{FD}$ are already 0.2 to 0.3 fm higher than ours, it seems that the present data would favor the results of Brissaud *et al.* and Greenlees *et al.* rather than those of Boyd *et al.*

## VI. CONCLUSION

For $\alpha$-particle scattering in the vicinity of the Coulomb barrier on 23 nuclei with atomic numbers between $Z=48$ and $Z=82$, we have shown by means of an optical-model analysis with Woods-Saxon potentials that the data yield unambiguously the interaction radius $R_{0.2}$. This interaction radius is the distance where the real nuclear potential is 0.2 MeV deep. It expresses the fact that all values of the depth $V$, half-way radius $R_{opt}$, and diffuseness $a$ of the real potential which obey the relationship $V\exp[(R_{opt}-R_{0.2})/a]=0.2$ MeV give a good fit to the data. Typical uncertainties (essentially statistical) on $R_{0.2}$ are ±0.03 fm.

An analysis of the same data in terms of density distributions and effective $\alpha$-nucleon interaction permits us to define for each nucleus a "fixed-density" radius $R_{FD}$ at which the nucleon density is $2\times10^{-3}$ nucleon/fm$^3$. In addition to the error on $R_{0.2}$, the fixed-density radius $R_{FD}$ is subject to a model-dependent uncertainty which originates in the uncertainty on the $\alpha$-nucleon effective force as well as in the uncertainty on the functional form of the radial density distribution. In the case of $^{208}$Pb, the Hartree-Fock calculation of Negele[28] agrees with our data if we use an effective force of Gaussian shape $-U_0\exp(-K^2r^2)$ with $U_0=127$ MeV and $K=0.6$ fm$^{-1}$. These values were found by Sumner[27] to give a good agreement between the Negele calculation and 42 MeV $\alpha$-scattering data on $^{40}$Ca and $^{208}$Pb. Considering only this effective force gives then

$$R_{FD}=R_{0.2}-(3.06\pm0.03)\text{ fm},$$

while considering all effective forces given so far in the literature gives

$$R_{FD}=R_{0.2}-(3.11\pm0.14)\text{ fm}.$$

The comparison to other experimental information on nuclear densities is on the whole satisfactory though incomplete. The most direct comparison is with the analysis of $K^-$ absorption in the nuclear periphery, but it is not conclusive.

Finally the average variation of $R_{FD}$ with mass number is found to be in good agreement for spherical nuclei with the predictions of the droplet model,[39] which is taken as evidence that the surface thickness of spherical nuclei does not vary appreciably in the mass region from tin to lead.

## ACKNOWLEDGMENTS

This work has largely benefited from numerous discussions with Dr. J. S. Blair and Dr. A. M. Bernstein. We would also like to acknowledge interesting discussions with Dr. J. Randrup, Dr. S. Koonin, and Dr. P. Quentin.

*Present address: University of Cairo, Cairo, Egypt.
†Present address: Institut für Kernphysik der Universität zu Köln, Köln, Germany.
‡Present address: Centre de Recherches Nucleaires, Strasbourg-Cronenbourg, France.

[1]J. S. Blair, in *Lectures in Theoretical Physics* (Univ. Colorado Press, Boulder, 1966), Vol. VIIIC, p. 343.
[2]D. F. Jackson and C. G. Morgan, Phys. Rev. 175, 1402 (1968).
[3]B. Fernandez and J. S. Blair, Phys. Rev. C 1, 1145 (1970).
[4]E. Rutherford, Phil. Mag. 37, 537 (1919).
[5]G. Goldring, M. Samuel, B. A. Watson, M. C. Bertin, and S. L. Tabor, Phys. Lett. 32B, 465 (1970).
[6]Y. Eisen, E. Abramson, G. Engler, M. Samuel, U. Smilansky, and Z. Vager, Nucl. Phys. A236, 327

(1974).
[7]S. L. Tabor, B. A. Watson, and S. S. Hansen, Phys. Rev. C 11, 198 (1975); 14, 514 (1976).
[8]G. Igo and R. M. Thaler, Phys. Rev. 106, 126 (1957).
[9]P. R. Christensen and A. Winther, Phys. Lett. 65B, 19 (1976).
[10]D. Werdecker, Ph.D. thesis, University of Cologne, 1973 (unpublished).
[11]W. Brückner, J. G. Merdinger, D. Pelte, U. Smilansky, and K. Traxel, Phys. Rev. Lett. 30, 57 (1973).
[12]A. M. Bernstein, Advan. Nucl. Phys. 3, 325 (1969).
[13]D. F. Jackson and V. K. Kembhavi, Phys. Rev. 178, 1626 (1969).
[14]C. G Morgan and D. F. Jackson, Phys. Rev. 188, 1758 (1969).
[15]A. Budzanowski, A. Dudek, K. Grotowski, and A. Strzalkowski, Phys. Lett. B32, 431 (1972).
[16]D. Slanina and H. McManus, Nucl. Phys. A116, 271 (1968).
[17]G. W. Greenlees, G. J. Pyle, and Y. C. Tang, Phys. Rev. C 1, 1145 (1970).
[18]D. F. Jackson, Rep. Prog. Phys. 37, 55 (1974).
[19]H. Rebel, in *Proceedings of the International Symposium on Nuclear Structure, Balatonfüred, 1975*, edited by I. Fodor-Lovas and G. Palla (The Hungarian Physical Society, Budapest, 1976); in Proceedings of the Second Conference on Radial Shapes of Nuclei, Cracow, 1976 (unpublished).
[20]A. K. Kerman, H. McManus, and R. M. Thaler, Ann. Phys. (N.Y.) 8, 591 (1959).
[21]B. Tatischeff and I. Brissaud, Nucl. Phys. A155, 89 (1970).
[22]I. Brissaud, Y. Le Bornec, B. Tatischeff, L. Bimbot, M. K. Brussel, and G. Duhamel, Nucl. Phys. A191, 145 (1972).
[23]F. Petrovitch, H. McManus, V. A. Madsen, and J. Atkinson, Phys. Rev. Lett. 22, 895 (1969).
[24]R. Schaeffer, Nucl. Phys. A158, 321 (1970).
[25]C. J. Batty, E. Friedman, and D. F. Jackson, Nucl. Phys. A175, 1 (1971).
[26]P. Mailandt, J. S. Lilley, and G. W. Greenlees, Phys. Rev. Lett. 28, 1075 (1972); Phys. Rev. C 8, 2189 (1973).
[27]W. Q. Sumner, Ph.D. thesis, University of Washington, 1974 (unpublished).
[28]J. W. Negele, Phys. Rev. C 1, 1260 (1970).
[29]L. R. B. Elton, *Nuclear Sizes* (Oxford U.P., New York, 1961).
[30]J. Heisenberg, R. Hofstadter, J. S. McCarthy, I. Sick, B. C. Clark, R. Herman, and D. G. Ravenhall, Phys. Rev. Lett. 23, 1402 (1969).
[31]B. Tatischeff, I. Brissaud, and L. Bimbot, Phys. Rev. C 5, 234 (1972).
[32]P. E. Hodgson, *The Optical Model of Elastic Scattering* (Clarendon, Oxford, 1963).
[33]D. Royer, M. Dost, and H. Doubre, Z. Phys. 265, 371 (1973); private communication.
[34]J. R. Ficenec, L. A. Fajardo, W. P. Trower, and I. Sick, Phys. Lett. 42B, 213 (1972).
[35]L. S. Cardman, D. Kalinsky, J. R. Legg, R. Yen, and C. K. Bockelman, Nucl. Phys. A216, 285 (1973).
[36]P. L. Lee and F. Boehm, Phys. Rev. C 8, 819 (1973).
[37]G. Backenstoss and K. Goebbel, Nucl. Phys. 62, 449 (1965).
[38]L. R. B. Elton, *Nuclear Radii*, Landolt-Börnstein: Numerical Data and Functional Relationships in Science and Technology Series (Springer, Berlin, 1967), I/2.
[39]W. D. Myers and W. J. Swiatecki, Ann. Phys. (N.Y.) 55, 395 (1969); 84, 186 (1974).
[40]W. D. Myers, Nucl. Phys. A145, 387 (1970).
[41]E. H. S. Burhop, Nucl. Phys. B1, 438 (1967).
[42]E. H. S. Burhop, D. H. Davis, J. Sacton, and G. Schorochoff, Nucl. Phys. A132, 625 (1969).
[43]D. H. Davis, S. P. Lovell, M.Csejthey-Barth, J. Sacton, G. Schorochoff, and M. O'Reilly, Nucl. Phys. B1, 434 (1967).
[44]T. E. O. Ericson and F. Scheck, Nucl. Phys. B19, 450 (1970).
[45]C. E. Wiegand, Phys. Rev. Lett. 22, 1235 (1969).
[46]H. A. Bethe and P. J. Siemens, Nucl. Phys. B21, 589 (1970).
[47]Y. N. Kim, *Mesic Atoms and Nuclear Structure* (North-Holland, Amsterdam, 1971), p. 167.
[48]I. Sick, Phys. Lett. 44B, 62 (1973).
[49]A. M. Bernstein and W. A. Seidler, Phys. Lett. 39B, 583 (1972).
[50]G. Hauser, R. Löhken, H. Rebel, G. Schatz, G. W. Schweimer, and J. Specht, Nucl. Phys. A128, 81 (1969).
[51]H. Alvensleben, U. Becker, W. K. Bertram, M. Chen, K. J. Cohen, T. M. Knasel, R. Marshall, D. J. Quinn, M. Rohde, G. H. Sanders, H. Schubel, and S. C. C. Ting, Phys. Rev. Lett. 24, 792 (1970).
[52]R. N. Boyd and G. W. Greenlees, Phys. Rev. 176, 1394 (1968); R. N. Boyd, J. Fenton, M. Williams, T. Kruse, and W. Savin, Nucl. Phys. A162, 497 (1971).